Journal of Structural Geology 32 (2010) 362–376

Contents lists available at ScienceDirect

Journal of Structural Geology

journal homepage: www.elsevier.com/locate/jsg

Tertiary compressional overprint on Aptian–Albian extensional magnetic fabrics, North-Pyrenean Zone

Belén Oliva-Urcia [a], Teresa Román-Berdiel [a,*], Antonio M. Casas [a], Emilio L. Pueyo [b], Cinta Osácar [a]

[a] Departamento de Ciencias de la Tierra, Universidad de Zaragoza, 50009 Zaragoza, Spain
[b] Instituto Geológico y Minero de España, Zaragoza, Spain

ARTICLE INFO

Article history:
Received 30 July 2009
Received in revised form
21 January 2010
Accepted 24 January 2010
Available online 4 February 2010

Keywords:
Anisotropy of Magnetic Susceptibility
Extension
Compression
Overprint
Pyrenees

ABSTRACT

The Mauléon Basin constitutes part of the North-Pyrenean Mesozoic extensional basins inverted during Pyrenean (Late Cretaceous–Tertiary) orogeny. A structural and magnetic fabric study of the Aptian–Albian black marls of the Mauléon Basin (North-Pyrenean Zone) provides new data indicating that when there is an intense deformation associated with the compressional stage (formation of a pervasive foliation) the magnetic lineation is strongly controlled by the latter tectonic deformation recorded in the basin. However, some areas of the sedimentary basin can still preserve the primary extensional event, depending on its position with respect to basin margin faults and heterogeneous deformation areas. Structural and AMS data define a fabric transition from extensional fabrics indicating an approximate N–S extension in the central (inner) domain of the basin, where compressional deformation was moderate to NE–SW compressional fabrics in boundary domains close to the inverted faults, where compressional deformation was more important (k_{max} becomes nearly parallel to the main Pyrenean direction NW–SE). Consequently, fabrics in the Mauléon Basin can be interpreted as the result of the overprint of compressional deformation onto a primary extensional fabric, which in turn endures in the central domain of the basin. In spite of its complicated pattern, AMS is revealed useful when considering the long-term history of sedimentary basins undergoing several deformation events.

1. Introduction

A common application of the analysis of Anisotropy of Magnetic Susceptibility (AMS) is the study of deformation in weakly deformed rocks lacking visible markers of deformation (e.g. Sagnotti et al., 1999; Cifelli et al., 2004;Raposo et al., 2006). In sedimentary rocks, the AMS analysis has been largely used in the study of deformation in compressional scenarios, where the magnetic lineation is usually parallel to the fold axes or the strike of thrusts (e.g. Graham, 1966; Kligfield et al., 1983; Parés et al., 1999; Saint-Bezar et al., 2002; Robion et al., 2007). AMS analysis has also been applied in extensional basins, where the magnetic lineation coincides with the stretching direction (e.g. Alfonsi, 1997; Cifelli et al., 2005; Soto et al., 2007, 2008). Nevertheless, most deformed areas record successive deformational events, especially in inverted extensional basins, where an extensional stage is followed by a compressional stage. In these scenarios the AMS can be a useful tool to characterise the deformational history of rocks (see e.g. Gil-Imaz et al., 2000).

Recent AMS studies in inverted extensional basins, such as the Cabuérniga Cretaceous Basin (located within the Basque–Cantabrian basin, Western Pyrenees) in Soto et al. (2007) indicate that AMS records at the earliest stages after deposition and compaction of rocks, with the deformation overprint of the extensional setting. The magnetic lineation in these studies represents the stretching direction of the extensional stage of the basin, and this extensional magnetic fabric is preserved and not modified by subsequent tectonic events, except for sites with compression-related cleavage (Soto et al., 2007). The overprint of a later and compressional tectonic event can produce also internal deformation and the development of compression-related cleavage that modifies the primary magnetic fabric and records the compressional events (Housen and van der Pluijm, 1991; Parés and Van der Pluijm, 2002; Oliva-Urcia et al., 2009).

In this study we present new AMS data from the inverted extensional Mauléon Basin (Northern Pyrenees). The main difference with previously studied Mesozoic inverted basins (Soto et al., 2007) is the intense deformation associated with the Cretaceous–Tertiary compressional stage. This deformation gave rise to the formation of a pervasive foliation in the Albian black marls and through most of the Axial Zone (Choukroune and Séguret, 1973).

* Corresponding author. Tel.: +34 976 762127; fax: +34 976 761106.
E-mail address: mtdjrb@unizar.es (T. Román-Berdiel).

0191-8141/$ – see front matter © 2010 Elsevier Ltd. All rights reserved.
doi:10.1016/j.jsg.2010.01.009

Consequently, this study focuses on aspects related to changes in a primary (sedimentary or extensional) magnetic fabric during foliation development, and provides some clues about the behaviour of magnetic fabrics in this tectonic setting. Furthermore it establishes a relationship between magnetic fabric development and Mesozoic extensional or Tertiary compressional stage of deformation depending of their location in the basin and with respect to compressional structures. Reliability of the interpretation of AMS was supported by a rock-magnetic study. Observations in thin sections and X-ray diffraction analyses were done in order to characterise microstructures and mineralogy.

2. The North-Pyrenean basin: structural setting

The Pyrenees formed during convergence between the Iberian and European plates in latest Cretaceous to Oligocene times. Previously, rifting during the Triassic and the Jurassic resulted in the formation of a system of extensional basins, with a complex sedimentary evolution changing from terrestrial to lagoonal and finally to shallow marine sediments, and relatively homogenous facies throughout the Pyrenean realm (Bourrouilh et al., 1995; Biteau et al., 2006). The extensional stage is particularly well recorded in the North-Pyrenean area, the Basque–Cantabrian basin (Western Pyrenees) and the South-Pyrenean Central Unit (SPCU, southern Pyrenees), with similar evolutionary trends. During the continental break-up, opening of the Bay of Biscay and rotation of the Iberian Peninsula (Aptian and Albian times), the basement underwent fundamental changes that influenced the tecto-sedimentary evolution and the structure of the range (Peybernès and Souquet, 1984). From Lower Aptian to Lower Albian the formation of deep sedimentary basins (black marls with spicules and ammonites) corresponds to the creation of the European and Iberian margins between the Tethys to the east and the Bay of Biscay to the west (Peybernès, 1982a,b). These basins are approximately rhombic-shaped according to the lozenged or rectangular fault pattern in the basement (N 140, N 60, Peybernès and Souquet, 1984). Their genesis can be explained by a sinistral transtension connected to the rifting occurring at this time in the Bay of Biscay (Montadert and Winnock, 1971; Deregnaucourt and Boillot, 1982). Subsequent intracontinental oblique convergence generated basin inversion. Compression during the Late Cretaceous and Tertiary Pyrenean orogeny overprinted and partially masked the earlier history. During Alpine deformation south-verging NW–SE thrusts, folds and related cleavage form (Fig. 1). The thrusts affecting the Mesozoic cover initiated in the Triassic materials (Choukroune, 1976; Teixell et al., 2000).

We focused our study in the Mauléon Basin, a strongly subsiding basin that preserves most of the Mesozoic stratigraphy. The evolution of this sector of the Pyrenean chain is linked to the strike-slip or transtensional movement of the North-Pyrenean fault and the formation of deep basins (Johnson and Hall, 1989), which are filled with black marls, and interpreted to result by pull-apart mechanisms (Debroas, 1990). The rotation of Iberia during the opening of the Bay of Biscay has been recently constrained to Aptian times (Gong et al., 2008). The Aptian–Albian black marls reach thicknesses of 1500 m in the Mauléon Basin showing clearly the regression of sedimentation at the end of the Albian. At the bottom, these marls change laterally to Aptian marine platform limestones (BRGM, 1969). Overlying the black marls several turbiditic units were deposited in the North-Pyrenean realm during the Late Cretaceous. The depocenters for each turbiditic unit probably do not coincide, and the total sedimentary thickness is about 3000 m. Since the end of the Cretaceous, and during the tectonic inversion stage, the main sedimentation area shifted towards the southern foreland basin, located on the Iberian plate and later on towards the Aquitaine Basin.

The Mauléon Basin extends 50 km in N105E direction (Fig. 2a). The basin is divided into two sub-basins: the northern part of the basin is separated from the southern part by the Sarrance anticline in the Eastern sector (Fig. 2a and b). The present-day structure is defined by three main thrusts that follow the orientation of the basin (N105E), and from north to south they are Mailh Arrouy, Sarrance and Lakora (Dubos-Sallée et al., 2007). The Mailh Arrouy and the Sarrance thrusts can be interpreted as rooted in the Triassic, but they are probably related in depth with reactivated basement normal faults. The Lakora frontal thrust can be interpreted as the southern boundary of the Mesozoic extensional basins (Fig. 2b).

Structural observations (S_0, S_1, tension gashes) and sampling (oriented hand blocks for thin sections and standard drilled specimens for AMS) of a total of 40 sites were made. The black marls of the Mauléon Basin are affected by a Tertiary pervasive cleavage throughout the basin. Bedding and cleavage planes are subparallel in most measured sites. Bedding and cleavage show very different attitudes at three sites (LU26, LU29, ASP11; see Table 2 and Fig. 7f). In addition, tension gashes, which can be related to the Cretaceous extensional stage, (e.g. Sites 8, 14 and 32, see Fig. 11b) have been observed at some sites. Observations of thin sections under the optical microscope do not contribute with additional information because of the very small grain size and dark color of the samples due to hydrocarbon content.

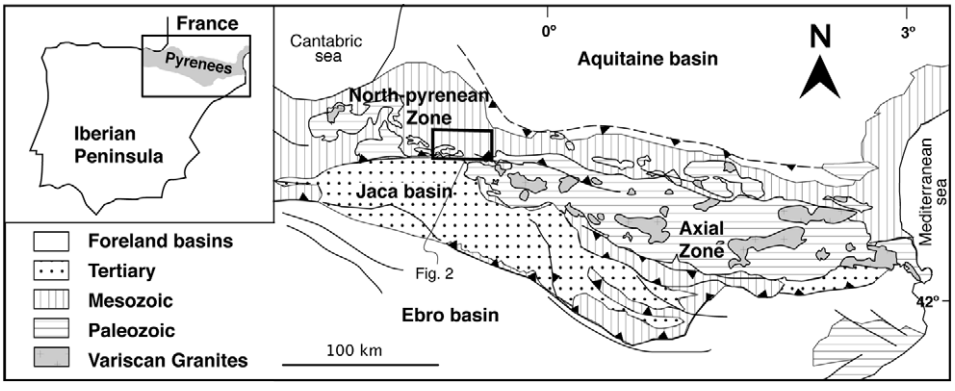

Fig. 1. Geological sketch map of the Pyrenees. The rectangle of the figure on the right shows the studied Mauleón basin (shown in Fig. 2 with more detail) (simplified from BRGM, 1969).

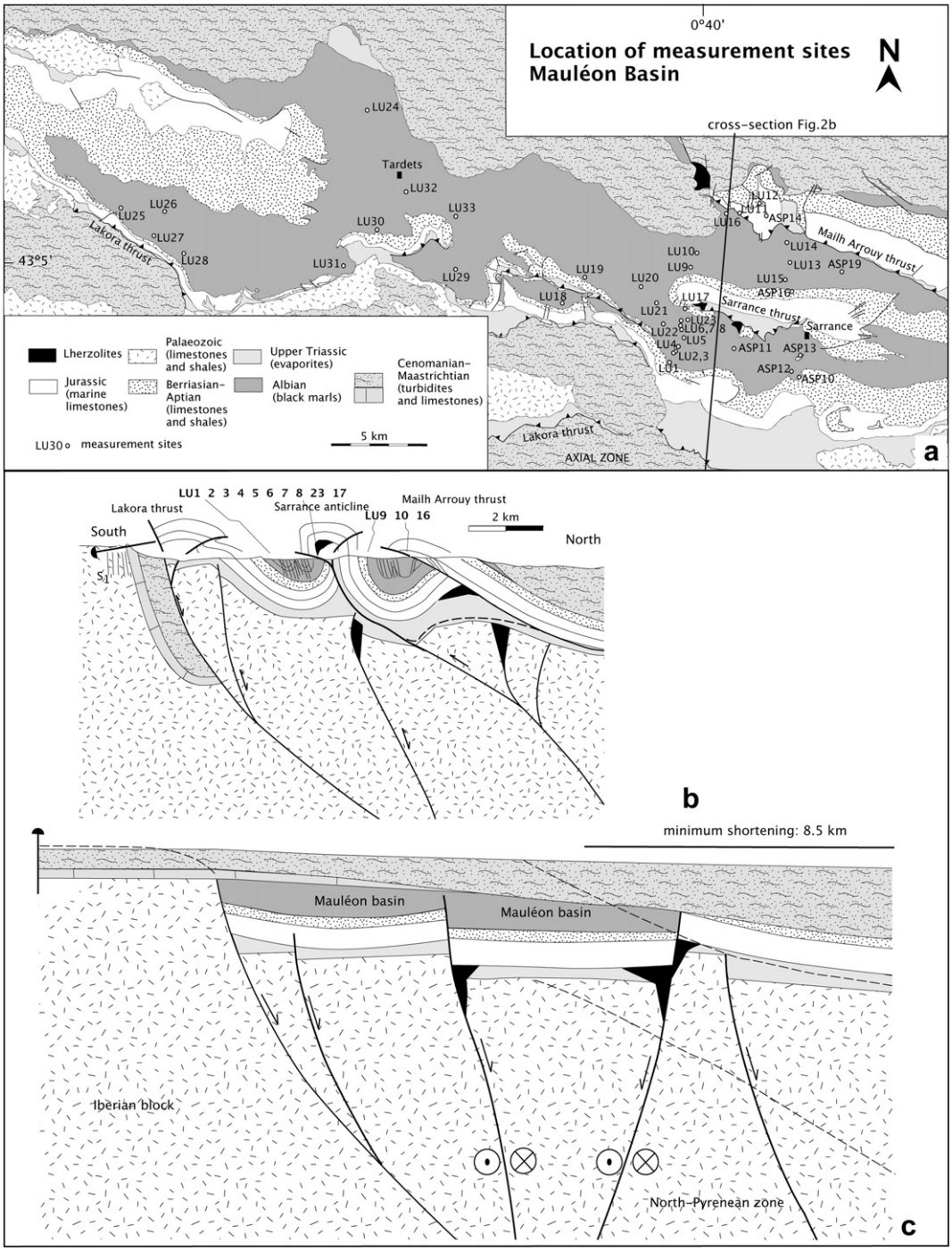

Fig. 2. (a) Geological map of the Mauléon Basin (Northern Pyrenees) with the location of measurement sites. (b) Geological cross-section (see (a) for location). (c) Restored cross-section.

3. Methodology

3.1. Mineralogy

In this study the analyses performed in order to control the mineralogy include: 1) X-ray diffraction (XRD) analyses and 2) optical observations under the SEM (Scanning Electron Microscope) and EDX (electron dispersive X-ray energy) analyses. Specifically, to have a better knowledge of the content of the magnetic carriers, two additional analyses have been performed: 3) temperature dependent susceptibility curves and 4) hysteresis loops and low-temperature measurements of the remanence (in DC field).

1) X-ray diffraction (XRD) analyses were performed at the University of Zaragoza with a Phillips PW 1729 diffractometer to control the mineralogy of the bulk sample. Semi-quantitative analysis was also carried out by means of the powder method, using Reference Intensity Ratios values (RIR) form literature (Davis et al., 1989).

2) Back scattered electron images were observed with a JSM-6400 Scanning Electron Microscope (SEM) at 20 kV at the University of Zaragoza. Semi-quantitative EDX analyses were performed with the INCA microanalyses software (Oxford Instruments). A piece of cobalt standard was used to calibrate the EDX signal at the beginning of every SEM session. The samples were cut perpendicular to the main foliation (S_1) to better observe the mineralogical assemblage, and are previously carbon coated.
3) The variation of susceptibility with temperature (χ–T curves) allows identification of strongly magnetic phases based on their Curie or Néel temperature. The Curie temperature (T_C) is sensitive to composition and defines the transition from ferromagnetic *s.l.* to paramagnetic ordering. T_C or TN (Néel or Curie temperature) can be determined from thermomagnetic curves by different methods. In this study the peak method has been used (see Lattard et al., 2006).

A KLY-3 kappabridge (working at 300 A/m and 875 Hz) combined with a CS-L/CS-3 apparatus (AGICO, Czech Republic) was used for the temperature dependent magnetic susceptibility (χ–T curves). Heating/cooling rates range between 11 and 14°/min respectively. The high temperature runs were performed in an argon atmosphere in order to avoid mineral reactions with oxygen during heating (flow rate of 110 ml/min). Some samples were also measured in airflow of the same rate. The raw data were corrected for the empty cryostat/furnace and normalized. The size of the samples is of few milligrams (20–30 mg).

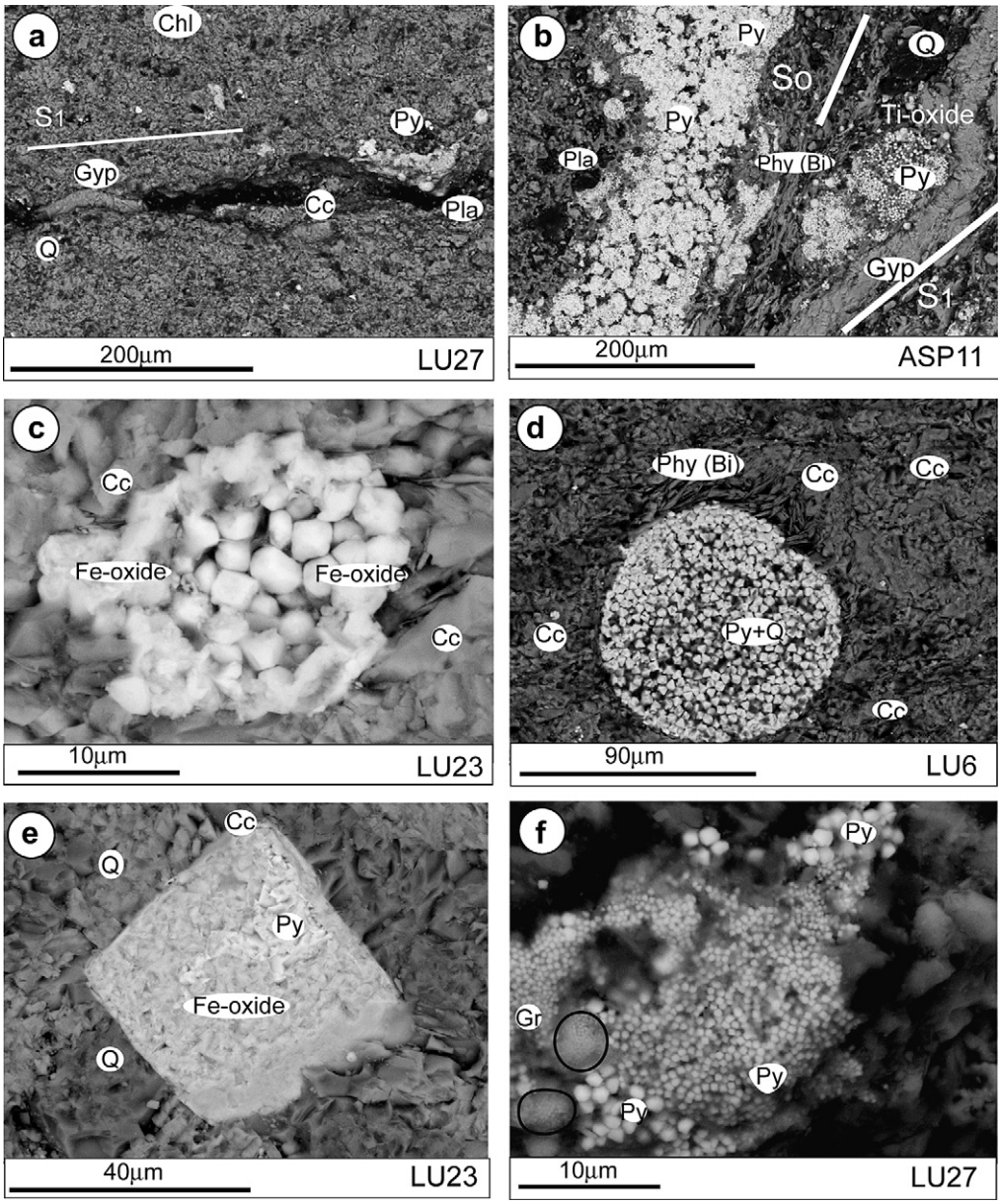

Fig. 3. (a) General aspect of the samples with a S_1 plane fill with gypsum. (b) General aspect of the samples with a S_1 plane fill with gypsum. Pyrite is abundant. (c) Octahedral iron oxides (magnetite) in a framboid surrounded by calcite grains. (d) Pyrite framboid disturbing the sedimentary attitude of phyllosilicates. Quartz is filling the voids of the framboids crystals. (e) Euhedral pyrite grain of 30 μm being replaced by magnetite (pseudomorph). (f) Different iron sulphides grain sizes and compositions. The smaller grains enclosed in a circle are iron enriched iron sulphides (closer to pyrrhotite–greigite composition). Py: pyrite, Gyp: gypsum, Cc: calcite, Q: quartz, Pla: plagioclase, Chl: chlorite, Phy: phyllosilicate, Bi: biotite, Gr: greigite composition (iron enriched Py), Fe-oxide: iron oxide, Ti-oxide: titanium oxide.

Table 1
Summary of magnetic scalar data.

Site	Lithology	K_m (μSI)	e ($\times 10^{-6}$)	P'	e	T	e	L	e	F	e
LU1	BM	176.6	3.633	1.057	0.002	−0.356	0.043	1.036	0.001	1.018	0.001
LU2	BM	118.9	2.489	1.034	0.001	−0.211	0.057	1.020	0.000	1.013	0.001
LU3	BM	105.2	4.152	1.061	0.008	0.330	0.122	1.015	0.001	1.042	0.008
LU4	BM	173.1	2.176	1.066	0.002	0.640	0.030	1.010	0.000	1.051	0.002
LU5	BM	188.0	3.534	1.083	0.002	0.591	0.015	1.015	0.000	1.062	0.002
LU6	BM	151.9	1.923	1.063	0.002	0.464	0.028	1.016	0.001	1.044	0.001
LU7	BM	111.2	2.377	1.038	0.000	−0.266	0.056	1.023	0.000	1.013	0.001
LU8	BM	72.5	2.308	1.045	0.001	−0.569	0.055	1.033	0.002	1.008	0.001
LU9	BM	176.2	5.227	1.033	0.001	0.208	0.038	1.012	0.000	1.020	0.001
LU10	BM	204.2	4.993	1.089	0.007	0.271	0.129	1.027	0.003	1.057	0.008
LU11	L	282.8	21.747	1.033	0.003	−0.191	0.112	1.020	0.003	1.011	0.001
LU12	L	197.7	8.393	1.044	0.002	0.125	0.070	1.019	0.001	1.024	0.001
LU13	BM	139.9	2.086	1.094	0.000	−0.037	0.022	1.047	0.001	1.044	0.001
LU14	BM	310.0	13.889	1.087	0.006	0.018	0.067	1.038	0.001	1.046	0.005
LU15	BM	122.0	11.375	1.092	0.013	0.478	0.105	1.013	0.002	1.071	0.010
LU16	BM	161.7	4.072	1.083	0.003	−0.202	0.042	1.048	0.001	1.032	0.002
LU17	BM	23.6	1.315	1.040	0.003	−0.483	0.042	1.028	0.002	1.010	0.001
LU18	BM	185.5	15.665	1.021	0.001	0.596	0.045	1.003	0.000	1.015	0.001
LU19	BM	247.3	5.830	1.048	0.003	0.127	0.053	1.020	0.001	1.027	0.002
LU20	BM	179.1	4.322	1.028	0.001	−0.086	0.050	1.015	0.001	1.012	0.000
LU21	BM	176.9	8.892	1.047	0.002	−0.528	0.046	1.034	0.002	1.010	0.001
LU22	BM	192.4	5.448	1.111	0.005	0.691	0.042	1.013	0.001	1.086	0.005
LU23	BM	55.7	1.459	1.054	0.003	0.001	0.064	1.026	0.002	1.026	0.002
LU24	BM	265.4	8.305	1.032	0.001	−0.057	0.079	1.016	0.001	1.014	0.001
LU25	BM	168.5	3.093	1.025	0.000	0.674	0.019	1.003	0.000	1.019	0.000
LU26	BM	115.8	6.668	1.015	0.000	0.013	0.079	1.007	0.000	1.007	0.000
LU27	BM	176.2	7.591	1.022	0.000	0.336	0.029	1.006	0.000	1.014	0.000
LU28	BM	156.6	9.262	1.031	0.002	0.623	0.041	1.005	0.000	1.024	0.002
LU29	BM	155.7	12.598	1.028	0.000	−0.393	0.033	1.019	0.000	1.008	0.000
LU30	BM	196.9	5.587	1.019	0.000	0.818	0.025	1.001	0.000	1.016	0.000
LU31	BM	167.5	8.437	1.012	0.000	−0.461	0.052	1.008	0.000	1.003	0.000
LU32	BM	193.2	10.244	1.029	0.002	0.292	0.060	1.008	0.000	1.019	0.002
LU33	BM	159.2	5.864	1.042	0.000	−0.233	0.016	1.025	0.000	1.016	0.000
ASP10	L	1.16	1.277	1.302	0.190	0.200	0.283	1.092	0.059	1.177	0.116
ASP11	BM	218.6	3.468	1.097	0.003	0.583	0.021	1.018	0.000	1.072	0.002
ASP12	BM	15.0	0.919	1.026	0.003	0.014	0.129	1.011	0.001	1.014	0.002
ASP13	L	−17.4	0.178	1.018	0.002	−0.400	0.259	1.012	0.002	1.005	0.002
ASP14	L	306.5	8.131	1.028	0.003	−0.377	0.134	1.019	0.003	1.007	0.001
ASP16	L	−16.9	0.343	1.009	0.003	−0.249	0.320	1.005	0.001	1.003	0.002
ASP19	BM	6.8	0.530	1.061	0.004	0.151	0.061	1.024	0.001	1.035	0.003

K_m magnitude of the magnetic susceptibility (in 10^{-6} SI), P' anisotropy degree, T shape parameter, L lineation, F foliation, e standard error. BM black marls, L limestones.

4) Hysteresis loops at room temperature and low-temperature measurements of the remanence under DC fields were performed with a SQUID MPMS Quantum design magnetometer (Magnetic properties measurements system) of the CSIC–University of Zaragoza. The maximum applied field for the hysteresis loops is 1.5 T. The remanence curves were measured after applying an SIRM of 2.5 T at 10 K and thermally demagnetizing the SIRM between 2.5 at 300 K. The samples consisted of few milligrams (20–30 mg).

3.2. AMS

Magnetic susceptibility is a physical property of materials and represents the capacity of the material to be magnetized in a given magnetic field. The magnetic susceptibility (K) is described by a second-rank tensor that relates the applied magnetic field (H) to an induced magnetization (M): $M = K \times H$. The AMS at room temperature in rocks depends mostly on crystallographic preferred orientation, shape of grains, composition and sometimes of distribution-interaction of magnetic minerals (Tarling and Hrouda, 1993). Three axes define the susceptibility ellipsoid: maximum (k_{max}), intermediate (k_{int}) and minimum (k_{min}). The orientations of these axes correspond to the eigenvectors of the susceptibility tensors and give the magnetic fabric. Other parameters that provide information about the shape and degree of magnetic fabric development are: the magnetic lineation ($L = k_{max}/k_{int}$), magnetic foliation ($F = k_{int}/k_{min}$); the corrected anisotropy degree, P', reflects the intensity of the preferred orientation of minerals in most cases, and the parameter T is the shape parameter, the prolate shapes are $-1<T<0$ and the oblate ellipsoids are when $1>T>0$. P' and T parameters are defined as in Jelinek (1981).

A total of 40 sites with an average of 15 specimens per site were drilled in the field with a portable drill. Structural observations for every site were also noted. The AMS was measured on standard specimens (2.5 cm in diameter, 2.1 cm in height) with a KLY3S (AGICO) in the Magnetic Laboratory of the University of Zaragoza. The average values for every site were calculated using Bingham distributions with Stereonet 6.3.0 (Allmendinger).

3.3. AMS at low temperature

Low-temperature AMS (LT-AMS) analyses were done on standard specimens with the KLY3S (AGICO) in the Magnetic Laboratory of the University of Zaragoza. The LT-AMS was analyzed in 4 selected sites to have a control on the minerals responsible for the observed fabric, specifically the magnetic lineation (k_{max}). Samples were cooled down in liquid nitrogen (77 K during 30 min) before the magnetic susceptibility was measured in air. Since the KLY3S measurements need three position changes, the sample is

immersed again in liquid nitrogen between positions for 10 min to allow the system to equilibrate between each measurement (as in Lüneburg et al., 1999). Each of the three positions measured in spinning mode takes about 20–30 s. The AMS determined by this measurement protocol was repeatable.

The magnetic susceptibility of paramagnetic minerals is enhanced at low temperatures following the Curie–Weiss law, so that at liquid nitrogen temperatures the k_{max} axes increase by a factor larger than the k_{min}. This produces a magnetic susceptibility intensity approximately 3.8 times higher than at room temperature, assuming a purely paramagnetic phases with paramagnetic Curie temperature around 0 K.

4. Results

4.1. Mineralogy

X-ray diffraction (XRD) analyses of 14 samples indicate that quartz and calcite are the most abundant minerals (quartz ranges between 27 and 55% and calcite/dolomite between 6 and 66%). Chlorite is the most abundant phyllosilicate with percentages between 5 and 54. Additionally, traces of micas, siderite, gypsum and feldspars are found in some samples (2–17%). Pyrite is the most abundant opaque mineral (9–22%), hematite is found in three samples with less than 3% and traces of greigite were also found at least in one sample.

The Scanning Electron Microscope (SEM) observations corroborate the XRD results (Fig. 3a, b). Most samples are siltstones. Their grain size ranges between tenths to tens of microns. The opaque grains under the microscope are mainly pyrite and in one sample magnetite is found replacing pyrite. As accessory minerals there are Ti-oxides and rare-earth element phosphates. As a late authigenic product gypsum is filling the S_1 planes in the samples where there are not iron oxides found (Fig. 3a, b). Pyrite shows a variety of forms, mostly framboids (10–100 μm in diameter (Fig. 3b–d) but also as isolated euhedral grains disperse within the matrix (Fig. 3a). The size of a single crystal ranges from less than 0.5 μm to 15 μm) (Fig. 3a, d). Larger euhedral pyrite crystals (40 μm) and small grains within framboids (less than 3 μm) are replaced by iron oxides (Fig. 3c, e). The framboids are disturbing the sedimentary texture of some phyllosilicates (Fig. 3d). Quartz is covering some pyrite framboids (Fig. 3d). The smaller pyrite crystals (less than 0.5 μm) show higher iron content than the larger crystals, which are closer to stoichiometric pyrite (Fig. 3f). The composition of the smaller grains is closer to greigite–pyrrhotite.

Phyllosilicates are short grains (10–15 μm), mostly micas (thinner: less than 5 μm) and chlorite (thicker grains: 20 μm). Some interleaved phyllosilicate grains are found (20 μm). Calcite shows sharp gain boundaries with less than 10 μm in size. Silicates vary from 30 to 50 μm (Fig. 3a).

4.2. Magnetic mineralogy and magnetic susceptibility

The studied rocks are characterised by their low bulk magnetic susceptibility, between −17 and 310 × 10^{-6} SI, Table 1. Low values in K_m are traditionally associated with paramagnetic minerals (e.g. Rochette, 1987), but recent works show the predominance of ferromagnetic carriers in rocks with low bulk susceptibility values (e.g. Hirt et al., 2004) or rocks with high ferromagnetic content (magnetite) but weakly orientated, which are not the main carriers of the AMS (Raposo and Berquó, 2008).

Temperature dependent susceptibility measurements have been done in eleven selected samples. The selected samples cover the whole susceptibility range and the different fabric types found in the Aptian–Albian black marls of the North-Pyrenean basin (Fig. 4). The temperature dependant susceptibility curves are very similar in all samples but one (LU23). The heating runs of the samples show a paramagnetic behaviour until circa 400 °C. The curve has a concave-hyperbolic shape in its initial part (see Fig. 4, the right side figures), with a steadily decrease of susceptibility as temperature increases until there is an abrupt increase in susceptibility from 400 to 580 °C and a sudden drop in susceptibility at this temperature. The heating run of sample LU23-5D ($K_m = 62 \times 10^{-6}$ SI) is the only one that shows an increase of the susceptibility as temperature rises to ca. 360 °C, indicating a non-paramagnetic behaviour. The increase in susceptibility between 400 and 580 °C is probably due to the formation of new magnetite during heating (T_c of magnetite is 580 °C). All cooling curves show a conspicuous increase in susceptibility, corroborating the creation of new magnetite in the heating run.

The comparison of the high field susceptibility (measured with the MPMS in the hysteresis loops) with the low field susceptibility (measured in sister samples in a Kappabridge KLY3S), suggests that the paramagnetic contribution range between 60 and 99% in most of the samples (4 samples out of 7), whereas ferrimagnetic contribution occurs in the rest of the samples (Fig. 5a).

The measurement of the remanence at low temperature in the MPMS shows the typical paramagnetic behaviour at low

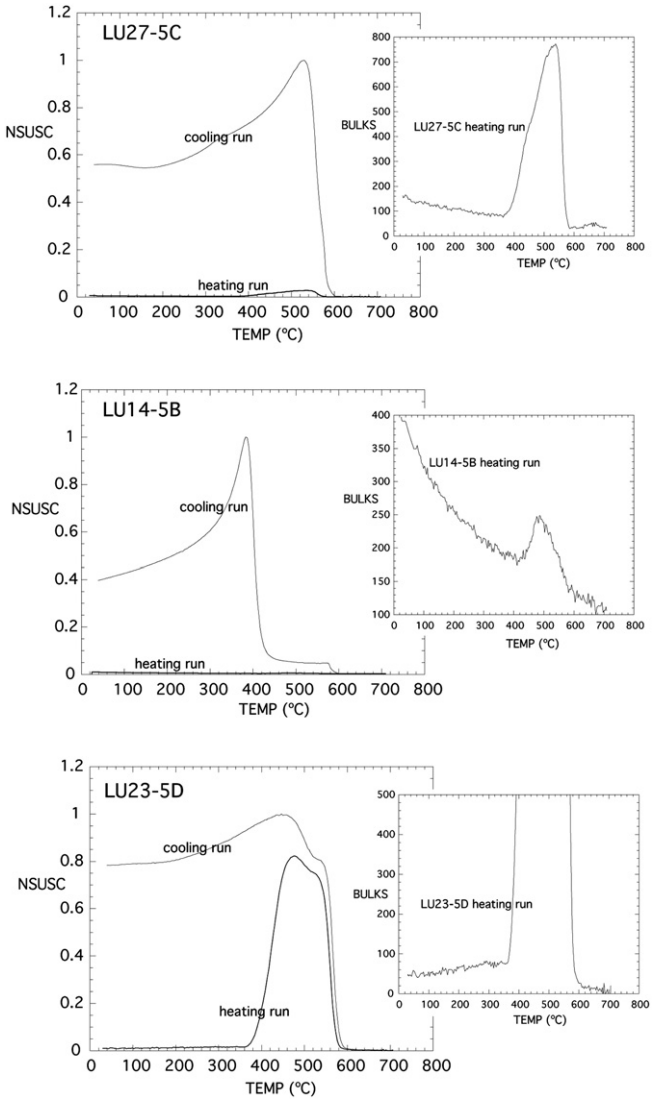

Fig. 4. Temperature dependent susceptibility curves of three representative specimens of the black marls. NSUSC: normalized susceptibility, BULKS: bulk susceptibility.

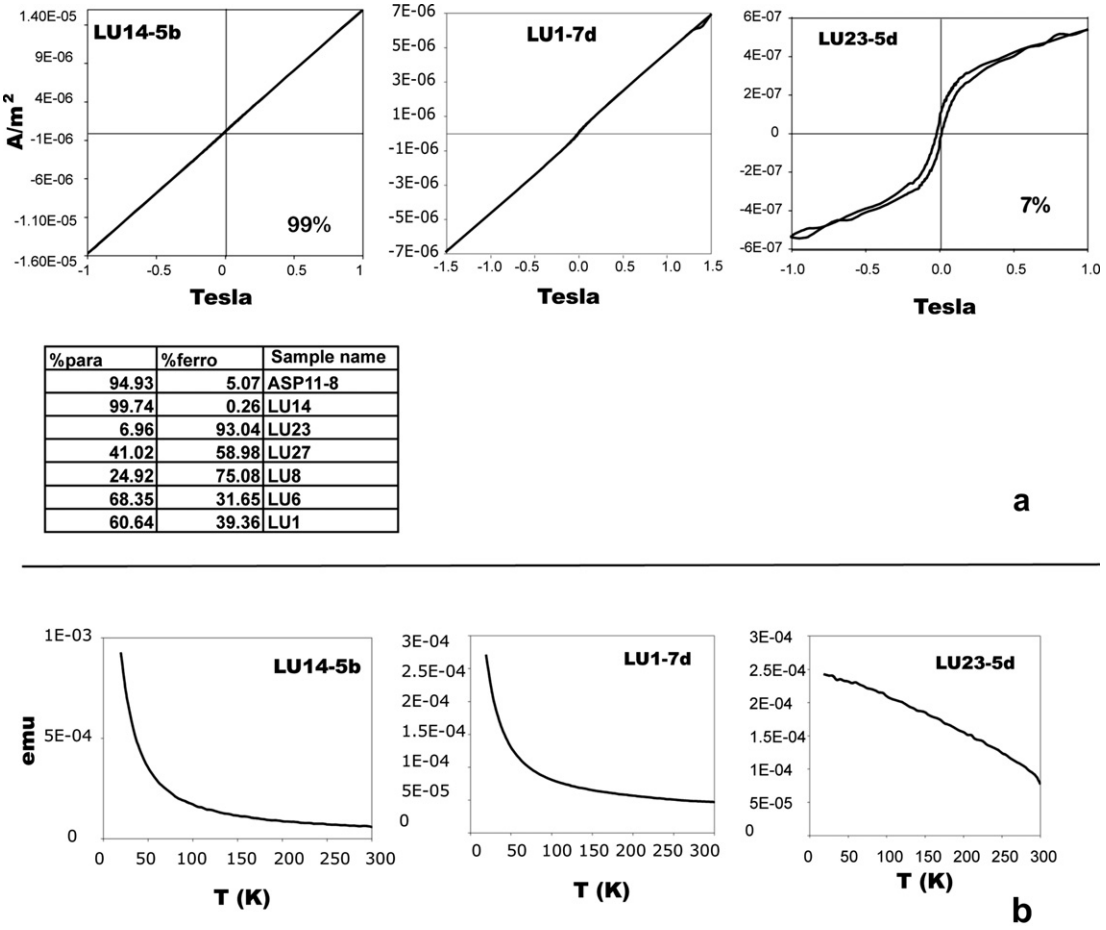

%para	%ferro	Sample name
94.93	5.07	ASP11-8
99.74	0.26	LU14
6.96	93.04	LU23
41.02	58.98	LU27
24.92	75.08	LU8
68.35	31.65	LU6
60.64	39.36	LU1

Fig. 5. (a) Hysteresis loops, (b) low-temperature DC field measurements.

temperatures (<40 K) except for sample LU23, with the hyperbolic decay of the remanence as the temperature increases. No phase transitions are observed (Fig. 5b).

4.3. AMS data

From the diagrams where P', T and K_m are represented it can be observed that there is neither correlation between the corrected anisotropy degree and the bulk susceptibility (Fig. 6a), nor between the shape of the magnetic susceptibility ellipsoid and the bulk susceptibility (Fig. 6b). Moreover there is not relationship between the shape of the magnetic ellipsoid and the corrected anisotropy degree (Fig. 6d). These results indicate that the values of T and P' are not influenced by petrographic variations, and the data of the magnetic ellipsoid provides information for the structural interpretation.

The corrected anisotropy degree P' varies between 1.009 (site ASP16) and 1.111 (site LU22). Site ASP10 (limestones), with an anomalous high P' value of 1.302, is not represented in Fig. 6. The anomalous value of P' can be related to values of the bulk susceptibilities near zero. Between -5 and $+5 \times 10^{-6}$ SI values of K_m, Hrouda (2004) recommends to avoid quantitative interpretation of AMS. The 78% of the sites show a corrected anisotropy degree lower than 1.08 (Table 1, Fig. 6a and d). The shape parameter T of the magnetic ellipsoid shows a large rank of variability, from strongly oblate ellipsoids to prolate fabrics (Fig. 6b and d). The Flinn diagram (Fig. 6c) shows stronger eccentric values of F (1.09) than L (1.05), confirming the information obtained from the T value.

Concerning the orientation of the magnetic ellipsoid axes, most sites can be grouped into five types (representative AMS plots are shown in Fig. 7). The first type (Fig. 7a) shows a triaxial susceptibility ellipsoid: all three principal susceptibility axes are well grouped, the minimum susceptibility axis k_{min} is almost perpendicular to the bedding/cleavage planes and a well-defined magnetic lineation appears. In 40% of sites this type of magnetic ellipsoid has been found. The second type (Fig. 7b) also shows a triaxial susceptibility ellipsoid, but the minimum susceptibility k_{min} is oblique to the bedding/cleavage planes. 13% of sites show this type of ellipsoid. The third type (Fig. 7c) refers to an oblate magnetic ellipsoid: the minimum susceptibility axes are perpendicular to the bedding/cleavage planes and the maximum and intermediate susceptibility axes are scattered within these planes. 20% of sites show this type of ellipsoid. Type 4 (Fig. 7d) refers to a prolate AMS ellipsoid: the maximum axes are clearly clustered and define a well-developed magnetic lineation while k_{int} and k_{min} form girdles perpendicular to k_{max}. Only three sites show this type of ellipsoid. Finally, Type 5 (Fig. 7e) has been defined in two sites where bedding and cleavage show very different attitudes. This type represents typical tectonic fabrics developed in cleaved regions (Graham, 1966; Kligfield et al., 1983). This magnetic fabric has k_{min} normal to cleavage and k_{int} and k_{max} well grouped (site ASP11) within the cleavage plane. The rest of sites (10%) do not fit in any of the former groups and show either k_{max} in a girdle distribution or scattered but not on the bedding/cleavage plane. Most of the limestones sites correspond to this last type. The five types of fabrics are distributed throughout the basin.

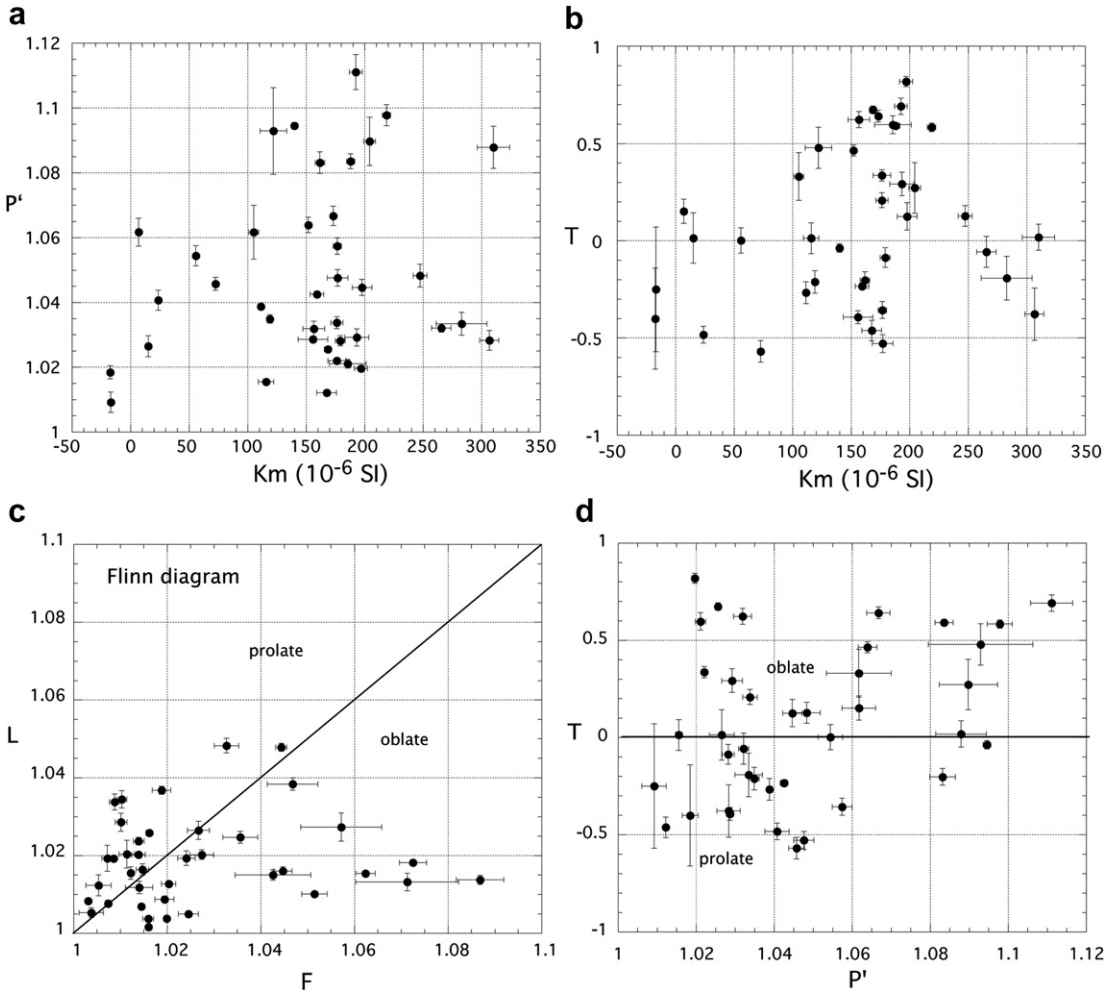

Fig. 6. (a) Corrected anisotropy degree (P') versus magnetic susceptibility (K_m). (b) Shape parameter (T) versus magnetic susceptibility (K_m). (c) Flinn diagram. (d) Shape parameter (T) versus the corrected anisotropy degree (P'). For all sites except ASP10.

Regarding the magnetic fabric, almost 70% of sites present a relatively high eigenvalue (E1 $>$ 0.8) of k_{max} (Table 2), which indicates a well-defined magnetic lineation.

4.4. AMS at low temperatures

The bulk susceptibility of the cooled samples is between 1.1 and 2.3 times the bulk susceptibility at room temperature. Since the susceptibility is measured in air, there are few seconds during which the sample warms up (temperature of the measurement is above 77 K). This time span can explain the lower increase in the bulk susceptibility respect to the K_m at room temperature, rather than a lower content in phyllosilicates (see Section 4.2 above). However, ratios lower than 3.8 but above 1 may also be related to either a partial contribution of ferromagnetic phases to the AMS or a paramagnetic phase with a paramagnetic Curie temperature above 0 K (chlorite and micas can have T_c around 30–35 K). Ratios around 1 are expected for ferromagnetic signal (Lüneburg et al., 1999).

Notwithstanding the lower increase of the bulk susceptibility at low temperature, the orientation of the k_{max} axes remains fixed between the low temperature and the room temperature measurements (Fig. 8). The samples selected to control the orientation of the magnetic ellipsoid at low temperatures have different values of susceptibility at room temperature (around 60–150 $\times$ 10^{-6} SI) and different shape of the magnetic ellipsoid (from ellipsoids with three axes well grouped to ellipsoids with k_{max} and k_{min} distributed in a girdle). In all these cases, the k_{max} axes at low temperature overlap with the k_{max} axes at room temperature.

5. Discussion and interpretation

5.1. Correlation between AMS fabric and structural elements

To restore the orientation of the ellipsoid before folding, we have used the bedding plane. Note that in 24 sites (out of 40) the bedding plane is parallel or subparallel to the penetrative cleavage planes (see Table 2 and Fig. 7f).

After the simple bedding plane restoration, the maxima of k_{max} (Fig. 9b) are subhorizontal and better grouped than in the non-restored stereogram (Fig. 9a). The better grouping of k_{max} after correction indicates that the magnetic fabric was fixed before folding. Considering the total set of data after tectonic correction, when bedding is horizontal, the distribution of k_{max} shows two maxima: the main maximum is oriented NW–SE (N130), and the secondary maximum is oriented N–S (N174) (Fig. 9b). In the same way, after the simple bedding plane restoration, the maxima of k_{min} (Fig. 9d) are subvertical and better grouped than in the non-restored stereogram (Fig. 9c).

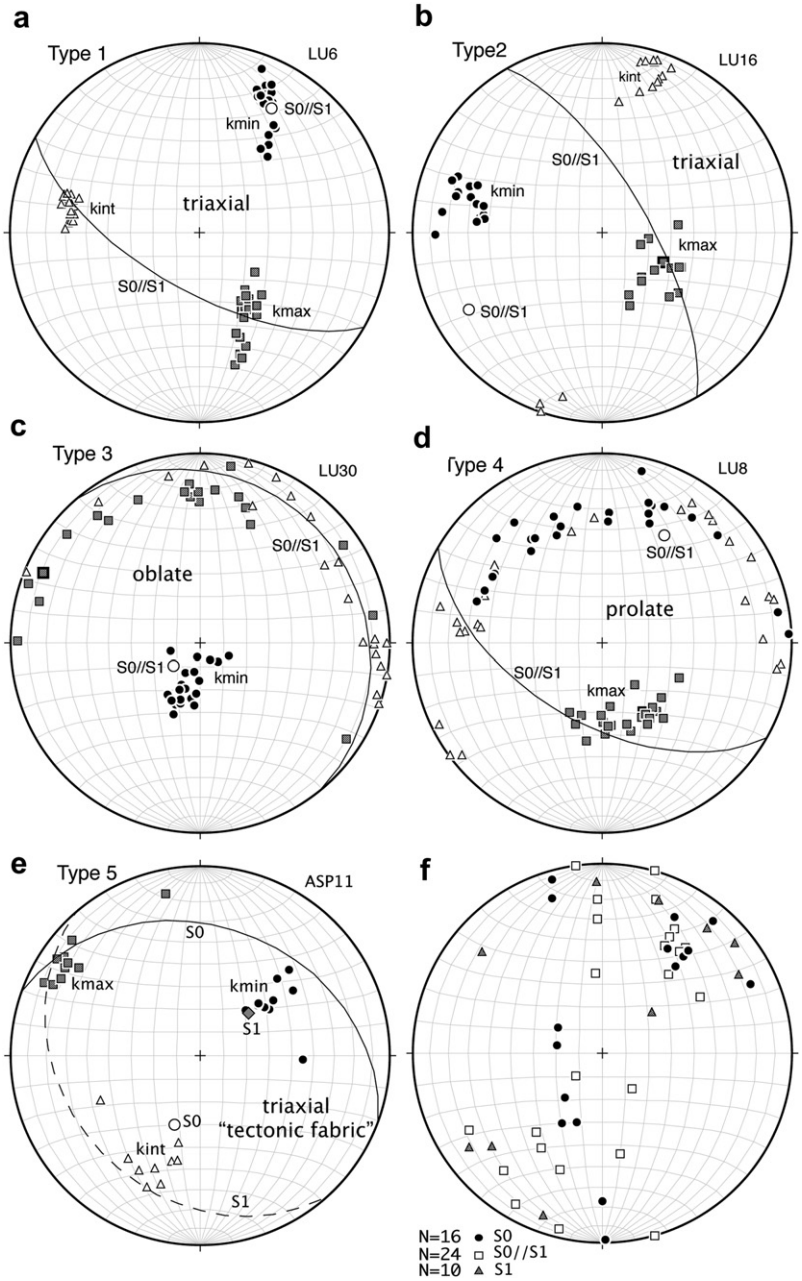

Fig. 7. (a–e) The five types of magnetic ellipsoids found in the studied area. (f) Stereoplot of poles to S_0 and/or S_1 for each site. Schmidt net, lower hemisphere projection.

Fig. 10 summarises in map view the orientation of the magnetic lineation of all sites after the tectonic correction together with the orientation of the present structural elements. The sites represented have a plunge of the k_{max} less than 26°. 35% of sites show a NW–SE magnetic lineation orientation. This orientation is parallel to the trend of the main present structures. 25% of sites show a N–S magnetic lineation orientation. This trend is consistent with the stretching direction of the basin in its extensional stage during the Early Aptian to Early Albian times (see below). 5% of sites show an intermediate magnetic lineation orientation (N150), 10% of sites show an E–W magnetic lineation orientation, and 5% of sites show an NNE–SSW magnetic lineation orientation.

In sites where extensional gashes have been measured (Fig. 11) there is a good correlation between the normal to the extensional gashes plane and the maximum axis of the susceptibility ellipsoid (k_{max}) when k_{max} shows a N–S direction after correction (e.g. site LU32, Fig. 11a). Nevertheless, in sites where k_{max} shows a NW–SE direction after tectonic correction there is no correlation with tension gashes (e.g. site LU14, Fig. 11a). As it has been previously shown, in some of the sites the k_{max} axes are parallel to the intersection lineation between cleavage and bedding, indicating also a partial conditioning of magnetic ellipsoid orientation by compressional structures.

Although a very clear pattern cannot be inferred, the sites showing N–S magnetic lineation orientation tend to be preferentially located at the inner parts of the basin (cores of the synclines and therefore younger rocks), and sites showing NW–SE magnetic lineation orientation are located at the boundaries of the basin (Figs. 10 and 12), later inverted as thrusts and reverse faults. These results suggest that although a pervasive cleavage has been developed during compressional stage, the earlier extensional magnetic fabric can be preserved at the inner parts of the basin, far from the structures reactivated during the compressional stage.

Table 2
Summary of magnetic directional data.

Site	k_{max} Dec/Inc	E1	E2	E3	k_{int} Dec/Inc	k_{min} Dec/Inc	E1	E2	E3	S_0	S_1	S_0/S_1
LU1	306/17	0.9704	0.0268	0.0029	059/55	207/32	0.7709	0.2237	0.0054			050/20N
LU2	305/21	0.8973	0.0907	0.0119	193/43	052/40	0.8069	0.1134	0.0797	130/50S		
LU3	142/17	0.9298	0.0433	0.0269	280/67	46/14	0.9382	0.0382	0.0236	155/75W	140/80W	
LU4	132/10	0.8687	0.1199	0.0113	237/65	044/22	0.9097	0.0883	0.0020	130/56S	150/72W	
LU5	131/22	0.9894	0.0085	0.0021	255/55	030/26	0.9807	0.0165	0.0028	130/60S	110/75S	
LU6	150/48	0.9638	0.0345	0.0017	281/31	028/26	0.9650	0.0340	0.0010			120/65S
LU7	140/42	0.9789	0.0164	0.0047	282/42	031/21	0.9378	0.0471	0.0152			120/60S
LU8	161/56	0.9464	0.0462	0.0074	255/03	347/33	0.7023	0.2834	0.0142			120/55S
LU9	107/09	0.8577	0.1341	0.0081	323/80	197/06	0.9813	0.0101	0.0086			106/90
LU10	092/74	0.6887	0.2897	0.0216	246/08	174/11	0.7160	0.2626	0.0315	118/70S	088/80S	
LU11	171/02	0.7435	0.1861	0.0704	064/86	263/07	0.7578	0.1785	0.0637			085/35S
LU12	144/19	0.6654	0.2795	0.0551	021/56	247/31	0.8077	0.1329	0.0593			130/45N
LU13	262/69	0.9781	0.0197	0.0022	036/15	130/14	0.9642	0.0290	0.0068			074/90
LU14	093/54	0.9813	0.0108	0.0079	219/23	320/26	0.9508	0.0437	0.0054	072/75S	040/72E	
LU15	154/54	0.6535	0.2389	0.1076	259/08	357/33	0.7054	0.1663	0.1283			088/70S
LU16	124/60	0.9565	0.0276	0.0159	017/09	283/27	0.9705	0.0196	0.0099			150/70E
LU17	089/18	0.9101	0.0777	0.0122	215/59	355/23	0.8395	0.1456	0.0090	074/85S		
LU18	124/07	0.7064	0.2434	0.0502	235/51	030/31	0.7144	0.2773	0.0082			088/60S
LU19	278/56	0.9398	0.0438	0.0164	181/05	087/34	0.9362	0.0411	0.0227			082/90
LU20	315/13	0.9282	0.0559	0.0159	146/75	047/04	0.9175	0.0723	0.0102			150/50W
LU21	147/08	0.8850	0.1045	0.0105	047/03	283/79	0.5747	0.3861	0.0393			130/45S
LU22	137/06	0.8741	0.0969	0.0290	236/53	039/34	0.8627	0.1138	0.0235			128/60S
LU23	198/45	0.9589	0.0233	0.0178	296/09	035/43	0.9371	0.0521	0.0108	122/55S		
LU24	047/64	0.7924	0.1597	0.0021	278/14	187/21	0.8303	0.1157	0.0540	130/80S		
LU25	118/16	0.8873	0.1023	0.0104	342/68	212/15	0.9847	0.0133	0.0020			120/81N
LU26	171/74	0.8988	0.0547	0.0465	276/03	007/15	0.8989	0.0694	0.0317	130/25N	130/75S	
LU27	119/04	0.9323	0.0585	0.0092	026/51	211/39	0.9262	0.0652	0.0085			123/50N
LU28	125/12	0.9298	0.0661	0.0041	010/63	221/24	0.9862	0.0122	0.0017			130/70N
LU29	320/05	0.9592	0.0282	0.0125	210/67	051/22	0.7641	0.2254	0.0105	010/20E	145/75E	
LU30	343/20	0.6480	0.3384	0.0136	079/10	196/71	0.9678	0.0256	0.0305			140/15N
LU31	285/40	0.8326	0.1460	0.0214	030/18	132/47	0.7850	0.1185	0.0965			110/55N
LU32	352/38	0.8775	0.0889	0.0336	095/14	198/46	0.8010	0.1757	0.0233	120/35N	140/65N	
LU33	328/41	0.9732	0.0235	0.0033	231/07	133/48	0.9840	0.0130	0.0030			080/45N
ASP10	292/22	0.6516	0.1892	0.1592	140/68	008/07	0.4675	0.2909	0.2417			109/75S
ASP11	306/15	0.9444	0.0516	0.0040	205/38	054/50	0.9576	0.0243	0.0181	110/32N	140/28W	
ASP12	121/21	0.7642	0.1885	0.0473	245/59	027/25	0.7655	0.1463	0.0882			127/57S
ASP13	048/54	0.8859	0.0939	0.0202	137/01	229/39	0.8022	0.1694	0.0284	030/22E		
ASP14	164/01	0.9334	0.0539	0.0127	270/76	073/16	0.6973	0.2713	0.0313	090/67N	110/80N	
ASP16	281/72	0.5346	0.3269	0.1385	049/36	136/14	0.5539	0.3152	0.1310	089/88N		
ASP19	066/67	0.6658	0.3147	0.0195	282/19	189/13	0.9163	0.0674	0.0162			104/85N

k_{max}, k_{int} and k_{min} mean (trend/plunge) considering a Bingham distribution; E1, E2, E3 eigenvalues, normalized to 1, corresponding to eigenvector E1 for k_{max} and k_{min}. S_0 bending, and S_1 foliation, measured in outcrops.

5.2. Regional implications of AMS results

The results obtained allow for some hypotheses about the regional evolution of the Mauléon Basin within the frame of the North-Pyrenean basins and their implications in internal deformation of materials filling the basins (Fig. 13). Since most samples were taken from a single lithology across the sedimentary basin, interpretation of AMS results can be done in terms of differential deformation during basin inversion and compression. In our opinion, some relevant facts must be taken into account for interpreting AMS results:

- Since continuous deformation occurred during the Pyrenean compression, AMS fabrics in the Mauléon Basin record the

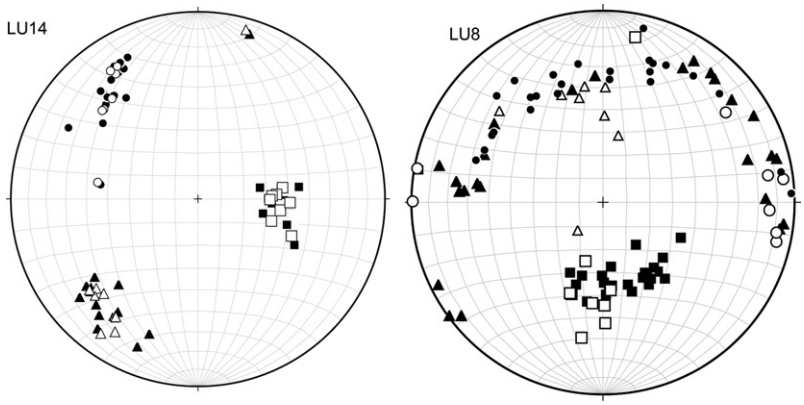

Fig. 8. Stereographic projection of AMS at room temperature (black symbols) and at low temperature (white symbols). Equal area, lower hemisphere projection.

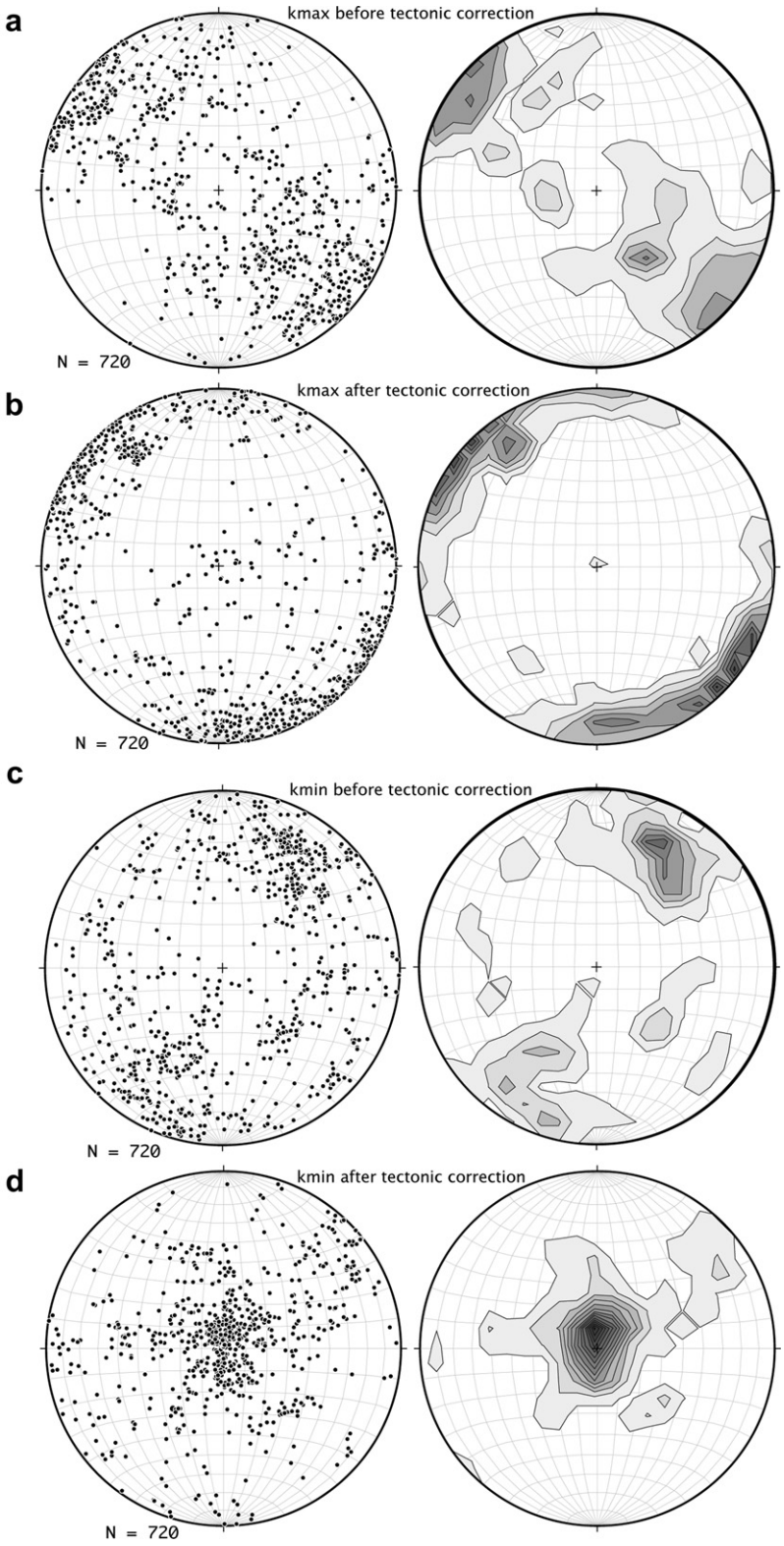

Fig. 9. (a) Stereoplot and density diagram of k_{max} before tectonic correction for all samples. (b) Stereoplot and density diagram of k_{max} after tectonic correction for all samples. (c) Stereoplot and density diagram of k_{min} before tectonic correction for all samples. (d) Stereoplot and density diagram of k_{min} after tectonic correction for all samples (Schmidt net, lower hemisphere projection, contour interval: 1%).

whole deformational history of the basin filling. Therefore, the orientation and shape of the magnetic susceptibility ellipsoid can be interpreted in terms of bulk deformation in different parts of the basin.

- Grouping of fabric orientation after tectonic correction (restoring bedding to the horizontal) and the orientation of k_{min} axes perpendicular to bedding strongly suggest that fabrics are related to processes predating the overall folding of

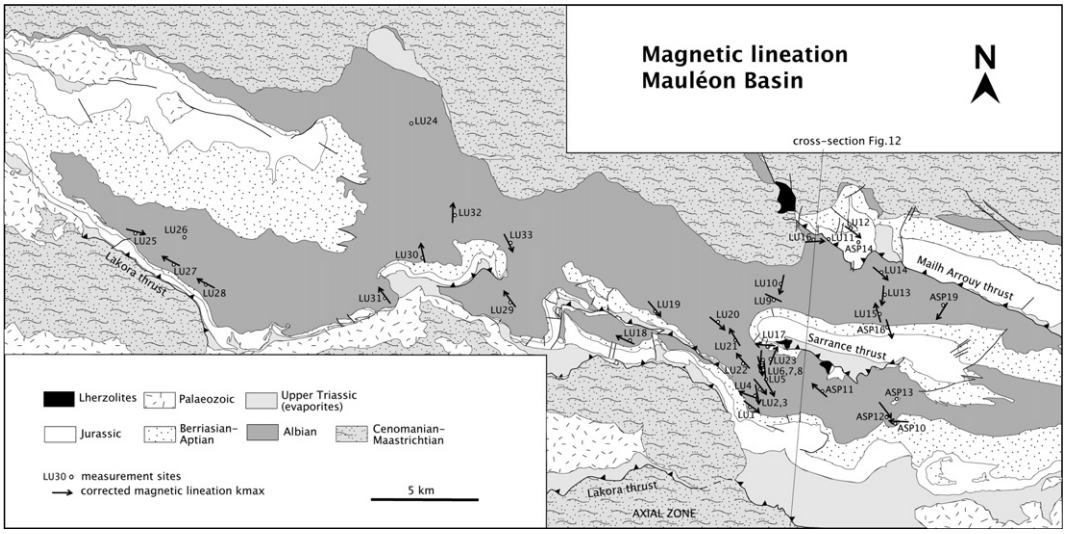

Fig. 10. Map of the studied area showing the orientation of magnetic lineations after bedding correction, except for sites where plunge of $k_{max} > 26°$.

the area. However, the parallelism between bedding and cleavage surfaces in many of the studied sites results in some ambiguity in the interpretation of timing of fabric formation.

- The structure of this sector of the North-Pyrenean Zone is characterised by upright tight folds and low-displacement thrusts with an overall southward vergence, resulting from the inversion of normal faults, whose geometry is not easy to reconstruct at present.

The Albian basins in the Northern Pyrenees have been interpreted as pull-apart basins resulting from the sinistral movement of the North-Pyrenean fault system (Fig. 13). Within this transtensional tectonic setting (Peybernès and Souquet, 1984; Debroas, 1990; Choukroune, 1992) the maximum extension direction was probably approaching the N–S direction (in present-day coordinates), probably varying to NW–SE, depending on the strike-slip/extension ratio and the particular geometry of faults and

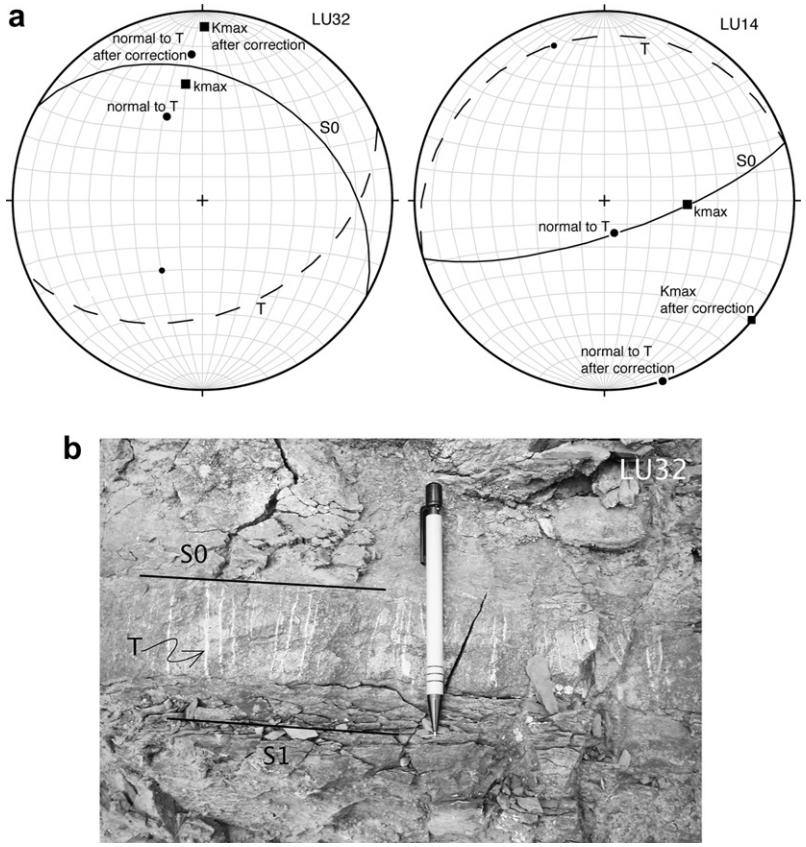

Fig. 11. (a) Stereoplots of S_0, tension gashes and k_{max} before and after bedding correction for sites LU14 (NW–SE magnetic lineation) and LU32 (N–S magnetic lineation) (Schmidt net, lower hemisphere projection). (b) Field aspect of tension gashes in site LU32.

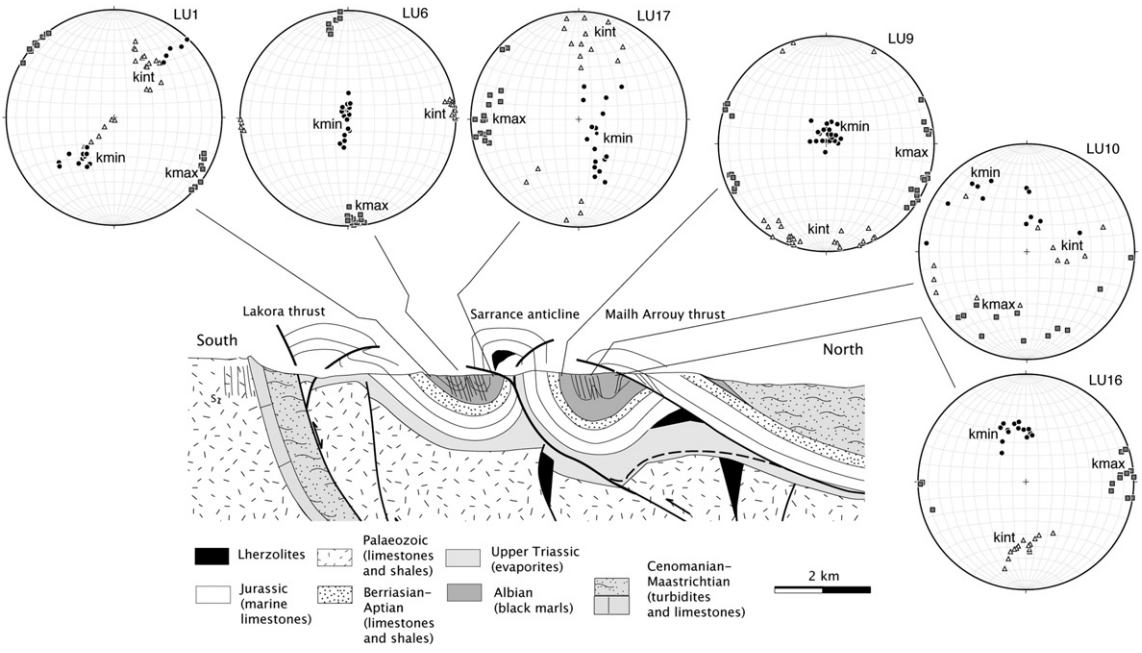

Fig. 12. Cross-section and stereoplots of representative magnetic fabrics at the inner/central part and at the boundary of the basin (Schmidt net, lower hemisphere projection).

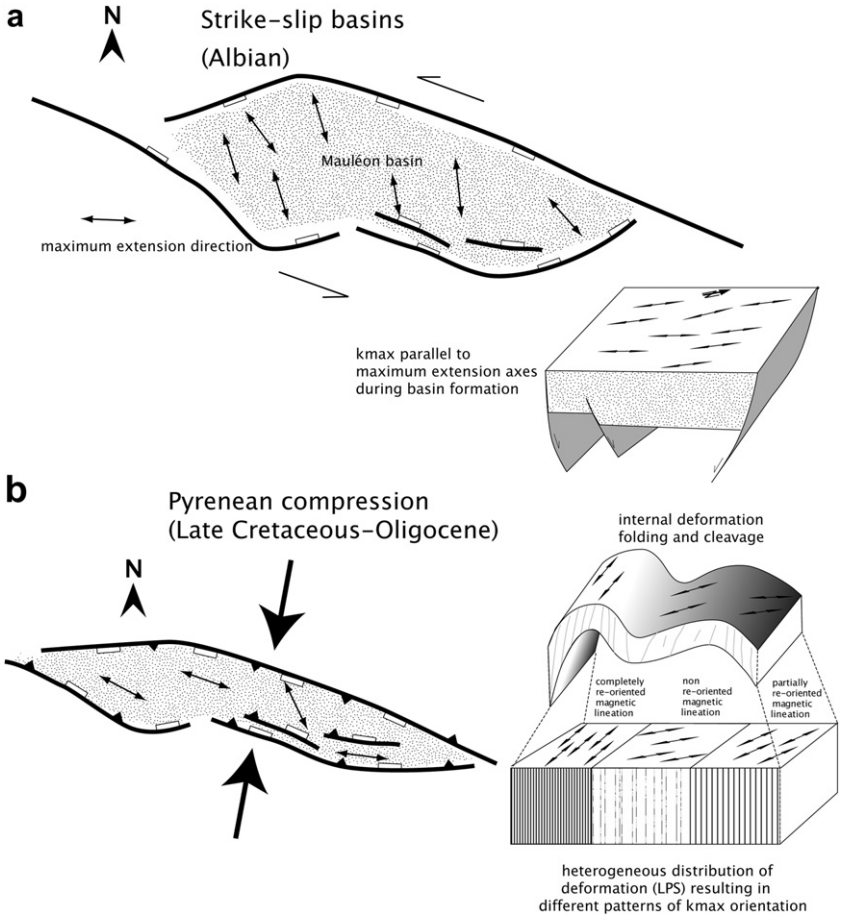

Fig. 13. Conceptual sketch showing the proposed hypothesis for the distribution of orientations of magnetic ellipsoids. During the Albian (a) basin formation under a strike-slip regime the orientation of k_{max} was probably nearly N–S, according to strain distribution in the pull-apart basins. During the Pyrenean compression (b) previous fabrics were deformed according to the NNE–SSW shortening direction. k_{max} axes became practically WNW–ESE in strongly deformed areas and approach the former extension direction in weakly deformed segments of fold limbs.

extensional steps between them. Fixation of the magnetic fabric in the first stages of sediment burial and diagenesis is a relatively common process (Larrasoaña et al., 2004) and occurrence of extensional magnetic fabrics has been documented in other Pyrenean basins (Soto et al., 2008). Therefore, we can hypothesise that, preserved or not after subsequent tectonic events, primary, extensional fabrics were recorded in the black marls at this stage.

Subsequent Pyrenean compression (Late Cretaceous–Tertiary) was oblique (NNE–SSW) to the former extension direction, and cleavage and folding formed at this stage (Choukroune, 1992). Therefore, the primary, extensional magnetic fabrics were probably modified during the process of cleavage formation. Heterogeneous deformation across the basin, probably related to the distance of the different parts of the basin to the inverted normal faults at the basin margins was the responsible for different degrees of modification of extensional fabrics (Fig. 13). According to models of magnetic fabric evolution (Graham, 1966; Kligfield et al., 1983), layer parallel shortening (LPS) predating folding is one of the most common processes in phyllosilicate-bearing rocks. When flattening resulting from cleavage formation is involved this process can be able to modify to a certain extent the previous extensional fabric. Consequently, fabrics in the Mauléon Basin can be interpreted as the result of the superimposition of extensional and compressional deformation. In panels strongly deformed during compression, k_{max} becomes nearly parallel to the main Pyrenean direction (WNW–ESE), thus becoming nearly parallel to the intersection lineation, whereas in other panels k_{max} shows an intermediate direction between N–S and the Pyrenean direction (Fig. 13). Folding contemporary to late with respect to cleavage of composite fabrics resulted in a complex directional pattern, complicated by the obliquity between the extensional, early fabric and the subsequent shortening direction.

AMS studies in the southern part of the central Pyrenees (Oliva-Urcia et al., 2009) have interpreted magnetic fabric orientation in Pyrenean direction as the result of folding and cleavage formation. In this area k_{max} axes oriented N–S to NNE–SSW are interpreted as the result of simple shear deformation linked to thrust sheet emplacement. However, the North-Pyrenean Zone shows particular features with respect to the Southern Pyrenees that prevent applying a similar model for AMS interpretation. The main differences lie in the very origin of sedimentary basins, linked to extensional or transtensional processes in the case of the North-Pyrenean basins and to foreland sedimentation during lithospheric flexure in the South-Pyrenean zone (Jaca-Pamplona and Tremp-Graus basins, see e.g. Capote et al., 2002). Therefore, fabrics in the younger rocks of the foreland, South-Pyrenean basins can be interpreted in a more straightforward way, but do not give information about the crucial timing of Iberian rotation in the evolution of the Pyrenean chain.

6. Conclusions

Our results indicate that when there is an intense deformation associated with the compressional stage (formation of a pervasive foliation), the magnetic lineation is strongly controlled by the latter tectonic deformation recorded in the basin. However, in some areas of the sedimentary basin the primary extensional event can still be preserved, depending on its position with respect to basin margin faults and heterogeneous deformation areas. Structural and AMS data define a fabric transition from extensional fabrics indicating an approximate N–S extension in the central (inner) domain of the basin, where compressional deformation was moderate to NE–SW, compressional fabrics in boundary domains, close to the inverted faults, where compressional deformation was more important. In spite of its complicated pattern, AMS is revealed as useful when considering the long-term history of sedimentary basins undergoing several deformation events.

Acknowledgements

The authors thank Sylvia Gracia for her help in measuring with the KLY3S susceptibility meter. Ana Arauzo and Enrique Guerrero are acknowledged for the measurements with the MPMS at the ICMA from the CSIC-Universidad de Zaragoza laboratory. This study has been financed by the research projects CGL2006-05817 and GCL2009-08969 (Spanish Ministry of Science and Innovation and FEDER funds). We acknowledge the careful and constructive revisions from Ann Hirt and an anonymous reviewer. BOU acknowledges the "Juan de la Cierva Postdoctoral Program" from the SMSI. Stereoplots were done with R. W. Allmendinger's Stereonet program.

References

Alfonsi, L., 1997. Paleomagnetic and anisotropy of magnetic susceptibility (AMS) analyses of the Plio-Pleistocene extensional Todi Basin, central Italy. Annali di Geofisica 40 (6), 1535–1549.
Biteau, J.J., Le Marrec, A., Le Vot, M., Masset, J.-M., 2006. The Aquitaine Basin. Petroleum Geoscience 12, 247–273.
Bourrouilh, R., Richert, J.P., Zolnaï, G., 1995. The north Pyrenean Aquitaine Basin, France: evolution and hydrocarbons. AAPG Bulletin 79 (6), 831–853.
BRGM, 1969. Carte Géologique de la France 1/80.000, feuille 239 (Mauléon), 2e édition. BRGM, Orléans la Source.
Capote, R., Muñoz, J.A., Simón, J.L., Liesa, C.L., Arlegui, L.E., 2002. Alpine tectonics I: the Alpine system north of the Betic cordillera. In: Gibbons, W., Moreno, T. (Eds.), The Geology of Spain. Geological Society of London, Special Publication, pp. 367–400.
Choukroune, P., 1976. Structure et évolution tectonique de la zone nord pyrénéenne. Analyse de la déformation dans une portion de chaîne à schistosité subverticale. Mémoires de la Société Géologique de France 55 (127), 116.
Choukroune, P., 1992. Tectonic evolution of the Pyrenees. Annual Review of Earth and Planetary Sciences 20, 143–158.
Choukroune, P., Séguret, M., 1973. Carte Structurale des Pyrénées, 1:500,000. Université des Sciences et Techniques du Languedoc (USTELA) and Elf-ERAP, Montpellier, France.
Cifelli, F., Rossetti, F., Mattei, M., Hirt, A.M., Funiciello, R., Tortorici, L., 2004. An AMS, structural and paleomagnetic study of quaternary deformation in eastern Sicily. Journal of Structural Geology 26, 29–46.
Cifelli, F., Mattei, M., Chadima, M., Hirt, A.M., Hansen, A., 2005. The origin of tectonic lineation in extensional basins: combined neutron texture and magnetic analyses on "undeformed" clays. Earth and Planetary Science Letters 235, 62–78.
Davis, B.L., Smith, D.K., Holomany, M.A., December, 1989. Tables of experimental reference intensity ratios, Table no. 2. Powder Diffraction Journal 4 (4), 201–204.
Debroas, E.J., 1990. Le flysch noir albo-cénomanien témoin de la structuration albienne à sénonienne de la Zone nord-pyrénéenne en Bigorre (Hautes-Pyrénées, France). Bulletin de la Société Géologique de France 6 (2), 283–285.
Deregnaucourt, D., Boillot, G., 1982. Nouvelle carte structurale du Golfe de Gascogne. Comptes Rendus de l'Académie des Sciences, Paris II 294, 219–222.
Dubos-Sallée, N., Nivière, B., Lacan, P., Hervouët, Y., 2007. A structural model for the seismicity of the Arudy (1980) epicentral area (Western Pyrenees, France). Geophysical Journal International 171, 259–270.
Gil-Imaz, A., Pocoví, A., Parés, J.M., Lago, M., 2000. Effect of tithostatic pressure and tectonic deformation on the magnetic fabric (anisotropy of magnetic susceptibility) in low-grade metamorphic rocks. Journal of Geophysical Research 105 (B9), 21,305–21,317.
Gong, Z., Langereis, C.G., Mullender, T.A.T., 2008. The rotation of Iberia during the Aptian and the opening of the Bay of Biscay. Earth and Planetary Science Letters 273, 80–93.
Graham, J.W., 1966. Significance of magnetic anisotropy in Appalachian sedimentary rocks. In: Smith, S. (Ed.), American Geophysical Union Monograph 10, pp. 627–648.
Housen, B.A., van der Pluijm, B., 1991. Slaty cleavage development and magnetic anisotropy fabrics. Journal of Geophysical Research 96, 9937–9946.
Hirt, A.M., Lowrie, W., Lüneburg, C., Lebit, H., Engelder, T., 2004. Magnetic and mineral fabric development in the Ordovician Martinsburg formation in the central Appalachian fold and Thrust Belt, Pennsylvania. In: Martin-Hernandez, F., Lünburg, C., Auboug, C., Jackson, M. (Eds.), Magnetic Fabric: Methods and Applications. Geological Society of London, Special Publication, vol. 238, pp. 109–126.
Hrouda, F., 2004. Problems in interpreting AMS parameters in diamagnetic rocks. In: Martín-Hernández, F., Lüneburg, C.M., Aubourg, C., Jackson, M. (Eds.), Magnetic Fabric: Methods and Applications. Geological Society of London, Special Publication, vol. 238, pp. 49–59.

Jelinek, V., 1981. Characterization of the magnetic fabric of rocks. Tectonophysics 79, 63–70.
Johnson, J.A., Hall, C.A., 1989. The structural and sedimentary evolution of the Cretaceous North Pyrenean Basin, southern France. GSA Bulletin 101 (2), 231–247.
Kligfield, R., Lowrie, W., Hirt, A., Siddans, A.W.B., 1983. Effect of progressive deformation on remanent magnetization of Permian redbeds from the Maritime Alps (France). Tectonophysics 98, 59–85.
Larrasoaña, J.C., Pueyo, E.L., Parés, J.M., 2004. An integrated AMS, structural, palaeo- and rock-magnetic study of the Eocene marine marls from the Jaca-Pamplona basin (Pyrenees, N Spain); new insights into the timing of magnetic fabric acquisition in weakly deformed mudrocks. In: Martín-Hernández, F., Lüneburg, C.M., Aubourg, C., Jackson, M. (Eds.), Magnetic Fabric: Methods and Applications. Geological Society of London, Special Publication, vol. 238, pp. 127–204.
Lattard, D., Engelmann, R., Kontny, A., Suerzapf, U., 2006. Curie temperatures of synthetic titanomagnetites in the Fe–Ti–O system: effects of composition, crystal chemistry, and thermomagnetic methods. Journal of Geophysical Research 111, B12S28. doi:10.1029/2006JB004591.
Lüneburg, C.M., Lampert, S.A., Hermann, I., Lebit, D., Hirt, A.M., Casey, M., Lowrie, W., 1999. Magnetic anisotropy, rock fabrics and finite strain in deformed sediments of SW Sardinia (Italy). Tectonophysics 307, 51–74.
Montadert, L., Winnock, E., 1971. L'histoire structurale du Golfe de Gascogne. In: Technip, (Ed.), Histoire structurale du Golfe de Gascogne. Collection Colloques et Séminaires – Institut Français du Pétrole, vol. 22, pp. VI, 1–18.
Oliva-Urcia, B., Larrasoaña, J.C., Pueyo, E.L., Gil, A., Mata, P., Parés, J.M., Schleicher, A.M., Pueyo, O., 2009. Disentangling magnetic subfabrics and their link to deformation processes in cleaved sedimentary rocks from the Internal Sierras (west central Pyrenees, Spain). Journal of Structural Geology. doi:10.1016/j.jsg.2008.11.002.
Parés, J.M., van der Pluijm, B.A., Dinarès-Turell, J., 1999. Evolution of magnetic fabrics during incipient deformation of mudrocks (Pyrenees, northern Spain). Tectonophysics 307, 1–14.
Parés, J.M., Van der Pluijm, B.A., 2002. Phyllosilicate fabric characterization by low-temperature anisotropy of magnetic susceptibility (LT-AMS). Geophysical Research Letters 29 (24). doi:10.1029/2002GL015459.
Peybernès, B., 1982a. Evolution spatio-temporelle des plates-formes carbonatées et des basins terrigènes dans le Crétacé inférieur des Pyrénées franco-espagnoles. Cretaceous Research 3, 57–58.
Peybernès, B., 1982b. Création puis évolution de la marge nord-ibérique des Pyrénées au Crétacé inférieur. Cuadernos de Geología Ibérica, Madrid 8, 983–1000.
Peybernès, B., Souquet, P., 1984. Basement blocks and tecto-sedimentary evolution in the Pyrenees during Mesozoic times. Geological Magazine 121, 397–405.
Raposo, M.I.B., McReath, I., d'Agrella-Filho, M.S., 2006. Magnetic fabrics, rock magnetism, catholuminescence and petrography of apparently undeformed Bambui carbonates from Sao Francisco Basin (Minas Gerais Statet, SE Brazil): an integrated study. Tectonophysics 418, 111–130.
Raposo, M.I.B., Berquó, Th.S., 2008. Tectonic fabric revealed by AARM of the proterozoic mafic dike swarm in the Salvador city (Bahia State): São Francisco Craton, NE Brazil. Physics of the Earth and Planetary Interiors 167, 179–194.
Robion, P., Grelaud, S., Frizon de Lamotte, D., 2007. Pre-folding magnetic fabrics in fold-and-thrust belts: why the apparent internal deformation of the sedimentary rocks from the Minervois basin (NE-Pyrenees, France) is so high compared to the Potwar basin (SW-Himalaya, Pakistan)? Sedimentary Geology 196, 181–200.
Rochette, P., 1987. Magnetic susceptibility of the rock matrix related to magnetic fabric studies. Journal of Structural Geology 9, 1015–1020.
Sagnotti, L., Winkler, A., Montore, P., Di Bella, L., Florindo, F., Mariucci, M.T., Marra, F., Alfonsi, L., Frepoli, A., 1999. Magnetic anisotropy of Plio-Pleistocene sediments from the Adriatic margin of the northern Apennines (Italy): implications for the time-space evolution of the stress field. Tectonophysics 311, 139–153.
Saint-Bezar, B., Hebert, R.L., Aubourg, C., Robion, P., Swennen, R., Frizon de Lamotte, D., 2002. Magnetic fabric and petrographic investigation of hematite-bearing sandstones within ramp-related folds: examples from the South Atlas Front (Morocco). Journal of Structural Geology 24, 1507–1520.
Soto, R., Casas-Sainz, A.M., Villalaín, J.J., Oliva-Urcia, B., 2007. Mesozoic extension in the Basque–Cantabrian basin (N Spain): contributions from AMS and brittle mesostructures. Tectonophysics 445, 373–394.
Soto, R., Casas-Sainz, A.M., Villalaín, J.J., Gil-Imaz, A., Fernández-González, G., Del Río, P., Calvo, M., Mochales, T., 2008. Characterizing the Mesozoic extension direction in the northern Iberian plate margin by anisotropy of magnetic susceptibility (AMS). Journal of Geological Society, London 165, 1007–1018.
Tarling, D.H., Hrouda, F., 1993. The Magnetic Anisotropy of Rocks. Chapman and Hall, 212 pp.
Teixell, A., Durney, D.W., Arboleya, M.L., 2000. Stress and fluid control on décollement within competent limestone. Journal of Structural Geology 22, 349–371.